Environmental
Science
Nano

PAPER

View Article Online
View Journal | View Issue

Check for updates

Cite this: *Environ. Sci.: Nano*, 2025, **12**, 1501

A novel route to synthesize Bi/β-Bi_2O_3@carbon: mechanism and performance for efficient degradation of organic pollutants†

Xia Zhang, Yifang Zhang, Xitong Yang, Jiaxin Han, Guifen Zhu and Jing Fan*

Metastable β-Bi_2O_3 exhibits high catalytic performance due to its suitable band gap, greater dielectric permittivity and conductivity. However, the difficultly in preparing β-Bi_2O_3 and β-Bi_2O_3 based materials is still a problem to be overcome. In this work, porous Bi/β-Bi_2O_3@carbon photocatalysts were prepared for the first time by using an atmosphere switching strategy during the post-cooling of metal–organic framework (MOF) pyrolysis. The crystal phase structure and composition of Bi/β-Bi_2O_3@carbon could be easily adjusted by simply switching the cooling atmosphere from N_2 to air when cooled to different temperatures. The photocatalytic activities of the material were evaluated by degradation of emerging pollutant fluorescent whitening agent (FWA) 351 under simulated solar light irradiation. It was observed that 10 mg L^{-1} FWA 351 was completely degraded within 4 h using the optimal photocatalyst. The mineralization efficiency reached 60% in 6 h. Active species trapping experiments confirmed that hole oxidation was responsible for the degradation of FWA 351. The increased activity was due to the improved visible light utilization resulted from the reduced bandgap of Bi/β-Bi_2O_3@carbon and the surface plasmon resonance effect of bismuth metal, as well as the facilitated interfacial electron migration and charge carrier separation through multi-interface transfer paths. The proposed strategy provides new ideas for designing and synthesizing functional materials. The efficient degradation and mineralization of FWA 351 with Bi/β-Bi_2O_3@carbon also confirmed its potential for future application in wastewater treatment.

Received 17th October 2024,
Accepted 13th December 2024

DOI: 10.1039/d4en00973h

rsc.li/es-nano

Environmental significance

Bi/β-Bi_2O_3@carbon was fabricated using an atmosphere switching strategy in the post-cooling of MOF pyrolysis. The crystal structure and composition could be easily adjusted by switching the cooling atmosphere from N_2 to air when cooled to different temperatures. Compared with traditional preparation methods of multi-component photocatalysts, this strategy has the advantages of simple procedure, low energy consumption and environmental friendliness. Synergistic effects of the reduced bandgap of Bi/β-Bi_2O_3@carbon, the surface plasmon resonance effect of bismuth metal, and the interfacial electron separation and migration through multi-interface transfer paths were responsible for the improved performance. Electron-deficient species attacked the fluorescent whitening agent 351 molecule, resulting in the breaking of C═C bonds and opening of aromatic rings, ultimately mineralizing into CO_2, H_2O and inorganic salts.

1. Introduction

Fluorescent whitening agents are widely used in manufacture of paper, textiles, detergents, plastics and other daily necessities due to the increasing pursuit of clean and white appearance of products.[1] However, most of these fluorescent whitening agents are difficult to biodegrade due to their stable chemical structure, which makes them escape easily from sewage treatment plants and eventually enter the environment.[2] Recently, these fluorescent brighteners have been reported to be harmful to aquatic organisms and humans due to their association with cancer, genetic mutations and eczema.[1,3] Hence, it is meaningful to seek effective removal strategies for such compounds in wastewater. Advanced oxidation technologies are useful for the removal of FWAs with high efficiency.[4–6] However, problems, such as the production of iron mud, the use of large amounts of chemical reagents in Fenton oxidation, and strict operating procedures for ozone oxidation, are still important factors hindering their wide applications. In recent years, photocatalytic technology powered by green sunlight energy has attracted increasing attention and considered to

---

School of Environment, Henan Key Laboratory for Environmental Pollution Control, Key Laboratory for Yellow River and Huai River Water Environment and Pollution Control, Ministry of Education, Henan Normal University, Xinxiang, Henan 453007, PR China. E-mail: fanjing@htu.cn; Tel: +86 373 3325719

† Electronic supplementary information (ESI) available. See DOI: **https://doi.org/10.1039/d4en00973h**

be a sustainable technology with potential application prospects. Nevertheless, such photocatalytic degradation of fluorescent whitening agents has not been reported so far, thus exploring this technology to remove FWAs from wastewater becomes a necessary research topic. For this purpose, the design and preparation of photocatalysts are the prerequisite for the engineering application of photocatalytic degradation of FWAs.

Bismuth oxide (Bi_2O_3) has attracted widespread attention because of its high electrical conductivity, narrow energy band gap, non-toxicity, high abundance and good stability. Bismuth oxide consists of high-temperature-stable α and δ phases and metastable β and γ phases.[7] Among them, metastable β-Bi_2O_3 has the smallest bandgap (1.48–2.58 eV) and exhibits higher activity than other crystalline bismuth oxides.[8] However, its bandgap is not narrow enough for the wider response range to visible light. To date, various strategies have been adopted to address these issues, including coupling it with carbon materials and precious metals as well as constructing heterogeneous structures with other semiconductors, through which the light harvesting and charge carrier dynamics can be effectively improved.[9–11] However, metastable β-Bi_2O_3 is easily transformed into a stable state when the temperature changes, which makes it difficult to prepare β-Bi_2O_3 by conventional methods. Therefore, development of novel β-Bi_2O_3 based photocatalysts and their facile preparation methods are of great significance.

Metal–organic frameworks (MOFs) exhibit unique organic–inorganic hybrid compositions and adjustable pore structures, and are multi-dimensional networks formed by the coordination and self-assembly of metal ions or clusters with organic ligands.[12,13] Based on these properties, MOF materials can be used as precursors or templates to construct various functional materials. In this context, Liu *et al.* reported MOF-5 as the template for porous carbon synthesis for the first time in 2008.[14] Since then, a variety of MOFs have been used to synthesize carbon, metal, metal oxide, metal sulfide and their composite materials by regulating the pyrolysis conditions.[15,16] These pyrolysis products not only retain some of the long-range order structures and porosity of MOF precursors, but also have the advantages of high purity, small particle sizes and easy to obtain single metal atoms. Moreover, periodic assembly of metal ions or clusters in MOFs can effectively avoid the agglomeration of metal based products.[17] In general, MOF derived metal oxide based nanomaterials have better catalytic activity than traditional precursors.[18] At present, the preparation of MOF-derived materials is mainly based on the organic skeleton of Zn, Cu, Co, Fe and Ni transition metals.[19–21] The trivalent bismuth ion has a unique-valence electron configuration ($4f^{14}5d^{10}6s^2$), large ionic radius and strong affinity to O and N atoms. Bismuth-MOF with metal Bi as a coordination center becomes an ideal candidate precursor or template due to its characteristics of high symmetry and abundant open pore structure and reactive sites.[22,23] For example, the derivative Bi@C nanocomposites were prepared with calcined Bi-MOF, by which the current response signal of the tested compound can be effectively improved due to its abundant surface reaction sites and large specific surface area.[24] Zhang *et al.* designed a plate-like Bi/α-Bi_2O_3–C heterostructure with boosted potassium storage performance through a structure-inheritance strategy derived from MOFs.[25] It is worth noting that although Bi/α-Bi_2O_3–C photocatalysts have been prepared through Bi-MOF pyrolysis, the preparation method reported so far has the disadvantages of a complicated process caused by multi-step pyrolysis or high energy consumption (600–900 °C). Furthermore, few cost-effective methods for controlling the crystal phase structure and composition have been reported, and the exact mechanism of Bi/β-Bi_2O_3@carbon materials derived from MOFs needs further investigation. Therefore, it is still a challenge to develop novel pyrolysis processes and explore the derivation mechanism of MOFs for the preparation of multi-functional materials.

In this work, for the first time, we prepared porous visible-light responsive Bi/β-Bi_2O_3@carbon photocatalysts by using the atmosphere switching strategy during post-cooling of MOF pyrolysis. The crystal phase structure and composition of Bi/β-Bi_2O_3@carbon could be easily adjusted by simply switching the cooling atmosphere from N_2 to air when cooled to different temperatures. To our knowledge, there is no literature report on the preparation of materials by using the atmosphere switching strategy in post-cooling of MOF pyrolysis. It was found that by using the optimal photocatalytic catalyst BBC-400, FWA 351 (10 mg L^{-1}) could be completely removed from water within 4 h, and the mineralization efficiency reached 60% in 6 h. Compared with the traditional preparation approaches of multi-component photocatalysts, the strategy reported here has the advantages of simple procedure, low energy consumption and environmental friendliness. To have a better understanding of the structure–performance correlation, the photocatalytic mechanism of Bi/β-Bi_2O_3@carbon for the removal of FWA 351 was also investigated from the crystal phase structure and composition, photoelectric and spectroscopic properties of the photocatalyst, and identification of active substances in the reaction.

2. Experimental

2.1 Materials

Methanol and bismuth nitrate pentahydrate were obtained from Sinopharm Chemical Reagent Co., Ltd. FWA 351 ($C_{28}H_{23}NaO_6S_2$) and terephthalic acid (H_3BTC) were provided by Macklin Biochemical Co., Ltd. All chemicals were analytically pure, and the water used was deionized water.

2.2 Synthesis of the CAU-17 precursor

The CAU-17 precursor was fabricated by a solvothermal method reported in the literature.[26] Typically, 150 mg of $Bi(NO_3)_3\cdot 5H_2O$ and 750 mg of H_3BTC were dissolved in 60 mL of methanol by ultrasound. Then, the solution was quickly poured into a 100 mL hydrothermal reactor and heated at 120 °C for 24 h. The white precipitate was collected and washed 4–5 times with methanol. Finally, the product was dried in a vacuum oven at 60 °C for 6 h.

2.3 Preparation of porous CAU-17 derived Bi/β-Bi_2O_3@carbon photocatalysts

Porous Bi/β-Bi_2O_3@carbon photocatalysts were prepared by a one-step pyrolysis of CAU-17 (Scheme 1). Typically, 0.5 g of CAU-17 was loaded in a quartz boat and placed in a tube furnace, and then heated at a rate of 2 °C min^{-1} to 600 °C and reacted in a nitrogen stream for 2 h at this temperature. When the furnace was cooled to specific temperatures (100 °C, 200 °C, 300 °C, 400 °C, 500 °C or 600 °C), the nitrogen atmosphere was switched to air atmosphere, and the sample was further cooled to room temperature in air atmosphere. The samples obtained at different atmosphere switching temperatures were respectively denoted as BBC-100, BBC-200, BBC-300, BBC-400, BBC-500 and BBC-600. For comparison, samples obtained from CAU-17 pyrolysis in air at 600 °C for 2 h and then cooled directly in air were labeled as BBC-air.

2.4 Characterization

X-ray diffraction (XRD) patterns were obtained using an X'Pert3 powder diffractometer [Cu Kα radiation (λ = 1.54056 Å)]. X-ray photoelectron spectroscopy (XPS) was performed using an ESCALAB 250Xi system. Morphology and elemental distribution were observed on a JSM-6390LV scanning electron microscope (SEM) and Talos F200X transmission electron microscope (TEM). The thermal behavior of materials was examined by thermogravimetric (TG) analysis using a STA449C thermal analyzer from 30 °C to 800 °C at a heating rate of 10 °C min^{-1} in a nitrogen flow of 100 mL min^{-1}. Using $BaSO_4$ as a reference, diffuse reflectance spectroscopy (DRS) testing was performed using a UV-3600 Plus spectrophotometer. Nitrogen adsorption–desorption was analyzed by Brunauer–Emmett–Teller (BET) using a BELSORP-Max physisorption analyzer. Photoluminescence (PL) spectra were obtained using a Cary Eclipse fluorophotometer. The surface charge properties of the materials in solution were analyzed using a Zetasizer Nano ZS analyzer.

2.5 Activity evaluation

FWA 351 was selected as the target pollutant to evaluate the photocatalytic activities of the materials, and is chemically stable because its molecular structure contains aromatic rings linked to strong electron-attracting sulfonyl groups. Photocatalytic experiments were conducted in a CEL-LAB500E photochemical reactor (Beijing Zhongjiao Jinyuan, China). The incident luminous flux was determined to be 3900 lx. Typically, 25 mg of the materials was dispersed in 50 mL 10 mg L^{-1} aqueous FWA 351 solution. Prior to illumination, the suspension was stirred in the dark for 40 min to ensure an adsorption–desorption equilibrium. Then, a 500 W xenon lamp was turned on to begin the photocatalytic reaction. Subsequently, 3 mL of reaction solution was extracted at regular intervals and centrifuged (10 000 rpm, 5 min). The absorbance at 348 nm was monitored using a UV-1800 UV-vis spectrometer to determine the concentration of FWA 351. The mineralization of FWA 351 by Bi/β-Bi_2O_3@carbon was tested using a Vario total organic carbon analyzer.

2.6 Electrochemical measurements

Electrochemical properties of photocatalysts were measured using an electrochemical analyzer (Chenhua CHI660C, Shanghai, China) in a three-electrode cell with 0.5 M Na_2SO_4 aqueous solution as an electrolyte. To prepare the working

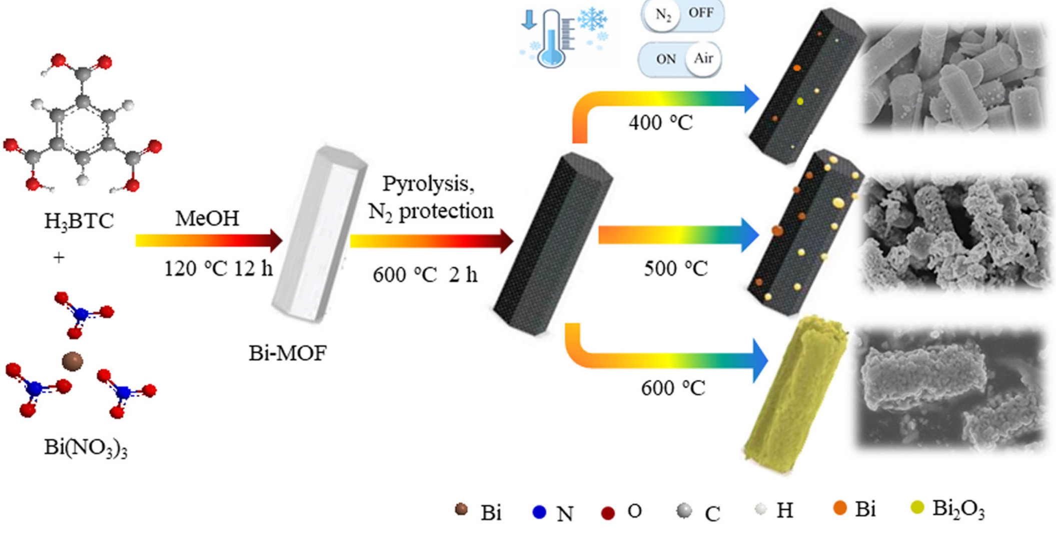

Scheme 1 Schematic diagram for the preparation of Bi/β-Bi_2O_3@carbon composite photocatalysts.

electrode, 5 mg of the synthesized samples were ultrasonically mixed with 10 μL of Nafion solution (5%) and 1200 μL of ethyl alcohol to form a slurry, which was then coated onto clean FTO glasses with an effective area of 0.5 × 0.5 cm^2. Then the electrode was dried in a vacuum chamber for 12 h at 60 °C. The calomel electrode and platinum wire separately acted as reference and counter electrodes.

Table 1 Content of components determined by the XRD Rietveld method

Sample	Bi (wt%)	Bi_2O_3 (wt%)	Carbon (wt%)
BBC-100	7.1	5.0	87.9
BBC-200	5.5	11.5	83.0
BBC-300	0.3	27.2	72.5
BBC-400	0.1	83.5	16.4
BBC-500	—	100.0	—
BBC-600	—	100.0	—

3. Results and discussion

3.1 Crystal phase composition and morphologies

The phase composition and crystal structure were analyzed by XRD. Fig. 1a shows that the positions of all the characteristic diffraction peaks were almost the same as those of the simulated XRD pattern of CAU-17 reported in the literature,[27] except for the slight difference in the relative intensity of the major diffraction peaks between the Bi-MOF and the simulated CAU-17. This was related to the preferred orientation and particle size of the material as well as the intensity of the light source. Fig. 1b shows the XRD patterns of Bi-MOF derivatives obtained under different conditions. It could be found that the diffraction peaks of the carbonized products (BBC-100, BBC-200, BBC-300, BBC-400 and BBC-500) were attributed to elemental bismuth (JCPDS No. 44-1246) and thermodynamically metastable tetragonal β-Bi_2O_3 (JCPDS No. 27-0050), and no other impurity peaks were found. Furthermore, the intensity of the diffraction peak of β-Bi_2O_3 and Bi increased and decreased with increasing atmosphere switching temperature, respectively. The reason might be that higher residual temperature and longer time air exposure could further oxidize more Bi components formed by the decomposition of the carbon skeleton to form β-Bi_2O_3.[28] It was noteworthy that a part of the β-Bi_2O_3 phase began to transform into stable monoclinic α-Bi_2O_3 (JCPDS No. 41-1449) with the further increase of atmosphere switching temperature (600 °C). A similar phase transition was observed in the BBC-air sample obtained by pyrolysis in air (labeled diamonds in Fig. 1b). Notably, metastable β-Bi_2O_3 has significantly higher photocatalytic activity than other crystalline Bi_2O_3 due to its more suitable band gap of ~2.58 eV, higher visible light utilization, and greater dielectric permittivity and conductivity.[29,30]

The Rietveld refinement method was used to analyze the XRD pattern and determine the percentage of the phase, and the results are shown in Table 1. It could be seen that with the increase of atmosphere switching temperature, the content of bismuth and carbon decreased, but that of Bi_2O_3 increased. When the temperature was regulated to 500 °C or 600 °C, the components were oxidized to Bi_2O_3. To confirm the results, the contents of elements in the material were determined using an Elementar Vario EL elemental analyzer (EA, Germany) and Perkin Elmer Optima 8300 inductively coupled plasma-mass spectrometer (ICP-MS, Japan), and the results are shown in Table S1.† It could be seen that the change of elemental composition was consistent with the results shown in Table 1. These results indicated that it was feasible to obtain a multi-component photocatalyst containing metastable β-Bi_2O_3, Bi and carbon with an adjustable component content by simply adjusting the atmosphere switching temperature during the post-cooling of MOF pyrolysis.

The surface morphology of the materials was surveyed by SEM. Fig. 2a and b show that a uniform hexagonal prism structure with a smooth surface, clear boundary and length of 5 μm was observed in the CAU-17 sample. After pyrolysis, except for the obvious change in the morphology of the BBC-600 sample, the other carbonized products (BBC-100, BBC-200, BBC-300, BBC-400, BBC-500) were similar to the original CAU-17, but the surface of the carbonized products became less smooth with many particles evenly embedded in the

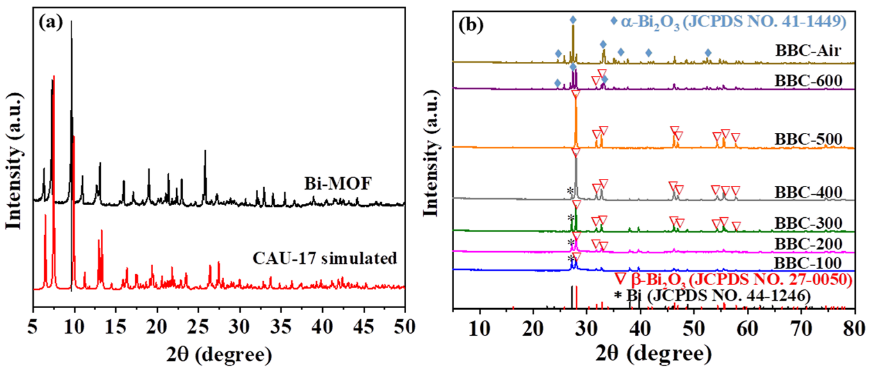

Fig. 1 XRD patterns of (a) CAU-17 and Bi-MOF, and (b) BBC-air, BBC-100, BBC-200, BBC-300, BBC-400, BBC-500 and BBC-600.

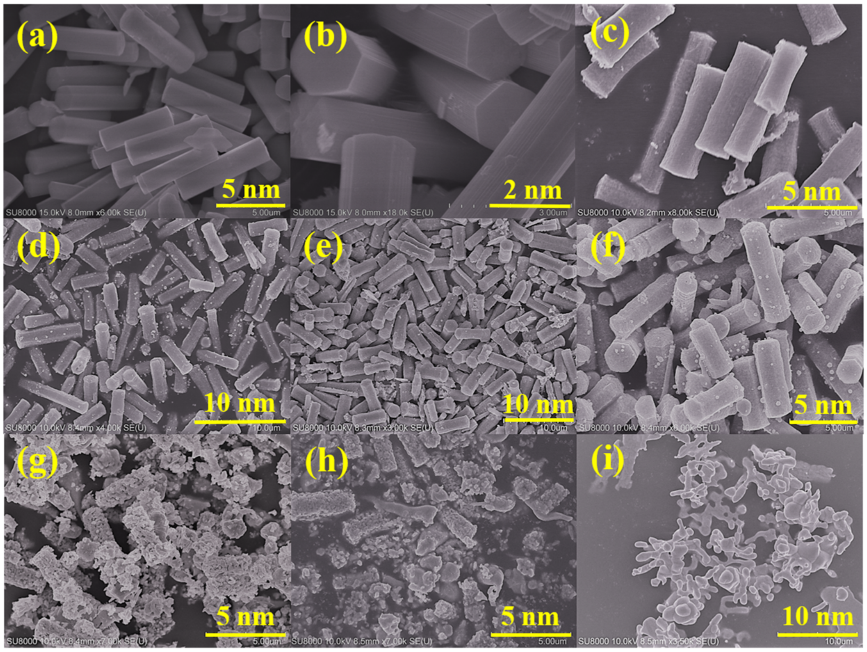

Fig. 2 SEM images of (a and b) CAU-17, (c) BBC-100, (d) BBC-200, (e) BBC-300, (f) BBC-400, (g) BBC-500, (h) BBC-600 and (i) BBC-air.

framework. The TG curves showed that the CAU-17 precursor began to decompose when the temperature rose to 400 °C (Fig. S1†), and the carbon in ligands was gradually converted to graphitized carbon, accompanied by the formation of metals and metal oxide particles, resulting in the roughness of the material surface.[31] In addition, metallic bismuth migrated to the surface and was further oxidized to form more Bi_2O_3 particles on the inner and outer surfaces of the materials, which agglomerated and grew larger with the Oswald ripening.[32] This result was confirmed by the fact that some fine particles adhered uniformly to the surface in Fig. 2c–h. The difference in the growth rate of Bi_2O_3 particles and the disappearance rate of carbon components may be the reason for maintaining the columnar structure at lower temperatures. In addition, due to the different initial temperatures when switching to the air atmosphere, the duration of air annealing of these samples must be different. With the increase of switching atmosphere temperature, the time required for the air calcination process of the BBC-*T* (*T* = 100, 200, 300, 400, 500, 600) samples gradually increased. High temperature accompanied by prolonged air exposure inevitably led to the oxidation of component carbon and elemental bismuth. For example, when the atmosphere switching temperature was higher than 500 °C, more carbon and bismuth metal components were oxidized, and parts of the columnar structure began to collapse. When the atmosphere switching temperature was increased to 600 °C, only a small amount of the columnar structure remained, and the collapsed material began to be sintered. The SEM image of the sample calcined in air at 600 °C (BBC-air)

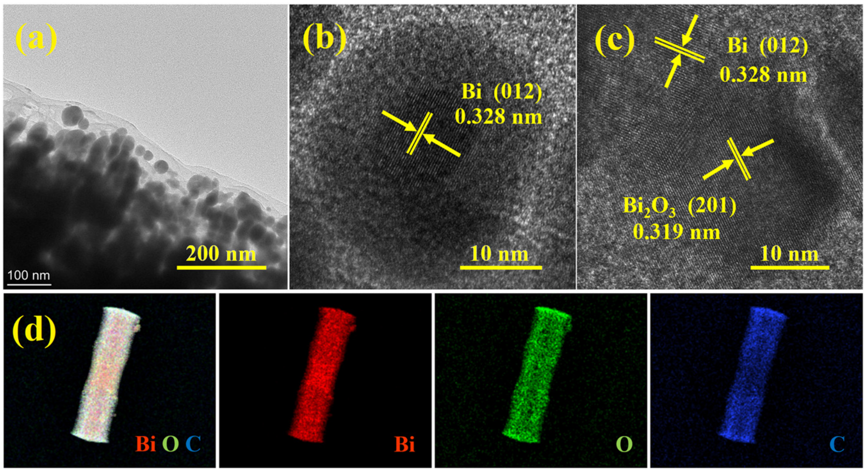

Fig. 3 (a) TEM image, (b and c) high-resolution TEM images and (d) elemental mapping images of BBC-400.

showed that the original columnar morphology and pore structure of CAU-17 were completely destroyed, forming a uniform staggered coral morphology (Fig. 2i).

To investigate the detailed microstructure, TEM images of BBC-400 were further analyzed. Many spherical particles were observed inside the material (Fig. 3a). High-resolution TEM images of the spheres exhibited two distinct lattice spacings of 0.328 and 0.319 nm (Fig. 3b and c), which were consistent with the (012) crystal plane of metal Bi and the (201) crystal plane of Bi_2O_3, respectively.[8,32] The results further confirmed that a part of metal Bi was oxidized after being in contact with air and formed spherical Bi_2O_3 particles. In addition, some particles have a core–shell structure composed of an unoxidized metal Bi core and Bi_2O_3 shell formed by air oxidation. The elemental mappings of the representative BBC-400 sample also revealed the uniform distribution of C, Bi and O elements in the composite (Fig. 3d).

XPS was used to analyze the surface elemental composition and chemical state of CAU-17, BBC-100, BBC-400, and BBC-600 (Fig. 4). The XPS survey spectra showed that all samples were composed of Bi, O and C elements (Fig. 4a), and the peak intensities of C 1s and Bi 4f decreased and increased with the increase of atmosphere switching temperature, respectively. As shown in Fig. 4b, the binding energy peaks at 159.5 eV and 164.8 eV in CAU-17 were attributed to Bi $4f_{7/2}$ and Bi $4f_{5/2}$ of the Bi–O bond, respectively.[33] After calcination, the position of the peak binding energy of Bi^{3+} in the obtained material BBC-100 shifted, indicating that the chemical environment of bismuth in the two materials changed significantly. In addition, the two weak peaks at 156.4 eV and 161.7 eV were signals of Bi $4f_{7/2}$ and Bi $4f_{5/2}$ of the Bi–Bi metal bond, respectively. The above results confirmed the coexistence of Bi_2O_3 and Bi components in composites.[34] Notably, no Bi–Bi signal was found in the BBC-400 and BBC-600 samples, which was inconsistent with the XRD results of metallic bismuth detected in BBC-400. The reason for this difference might be that most of the metallic bismuth on the superficial surface was oxidized to Bi_2O_3 at higher temperature, while metallic bismuth on the deep surface was undetectable due to the lower surface depth detected by XPS compared with XRD. In addition, the crystal conversion from β-Bi_2O_3 to α-Bi_2O_3 at higher temperature resulted in the wider lattice spacing of BBC-600, which was mainly responsible for the lower binding energy of BBC-600 than that of BBC-400.[35,36] The high resolution peaks of C 1s spectra (Fig. 4c) at 284.6 eV, 285.2 eV, 286.0 eV and 289.0 eV were ascribed to C═C (sp^2), C–C (sp^2), C–O and C═O, respectively.[37] The graphitization of the carbon component in the organic skeleton was beneficial for the separation and transport of charge carriers generated by the photo-excitation of materials. The two peaks at 531.4 eV and 533.5 eV in the O 1s XPS spectrum of CAU-17 were attributed to the Bi–O bonds and the O in bismuth–oxo clusters of CAU-17, respectively. The other peak at 531.8 eV was attributed to the chemisorbed H_2O/OH^- on its surface (Fig. 4d).[38] For the product after pyrolysis, the three characteristic peaks of the O 1s spectrum corresponded to oxygen atoms in the Bi–O bond (529.8 eV), hydroxyl groups or O_2 (532.0 eV) and adsorbed H_2O (533.6 eV), respectively.[39] These results further confirmed the successful preparation of the Bi/β-Bi_2O_3@carbon photocatalyst.

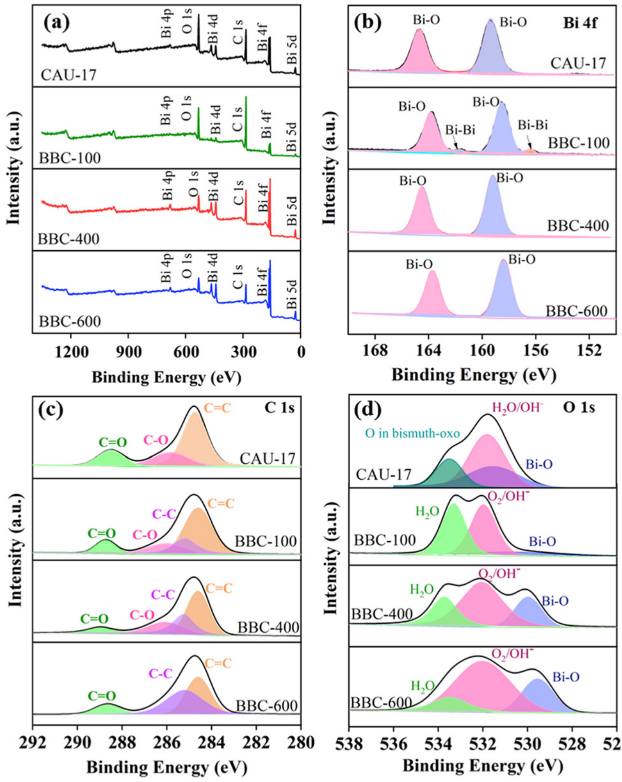

Fig. 4 (a) XPS survey spectra of CAU-17, BBC-100, BBC-400 and BBC-600. High resolution XPS spectra of (b) Bi 4f, (c) C 1s and (d) O 1s.

3.2 Pore structure, specific surface area and optical properties

N_2 adsorption–desorption isotherms were measured to analyze the pore properties and specific surface area of the prepared samples. As shown in Fig. 5a, CAU-17 showed a type-I adsorption isotherm, and the pore size distribution curve of CAU-17 in Fig. 5b also presented a narrow pore distribution with a peak value of about 0.7 nm, indicating the existence of micropores in the structure. Moreover, due to the collapse of a part of the carbon skeleton, the adsorption of BBC-100, BBC-200, BBC-300 and BBC-400 changed from type-I to type-III, and the pore size distribution changed from a micropore structure to coexistence of micropore and mesoporous structures. Thus, the total adsorption capacity and macro-molecule adsorption could be guaranteed.[40] The BET surface area of CAU-17 was measured to be 482.5 m^2 g^{-1}. After pyrolysis, the BET surface area of BBC-100, BBC-200, BBC-300 and BBC-400 decreased to 120.78, 112.4, 102.2 and 73.29 m^2 g^{-1}, respectively. In addition, at a higher temperature of the switching

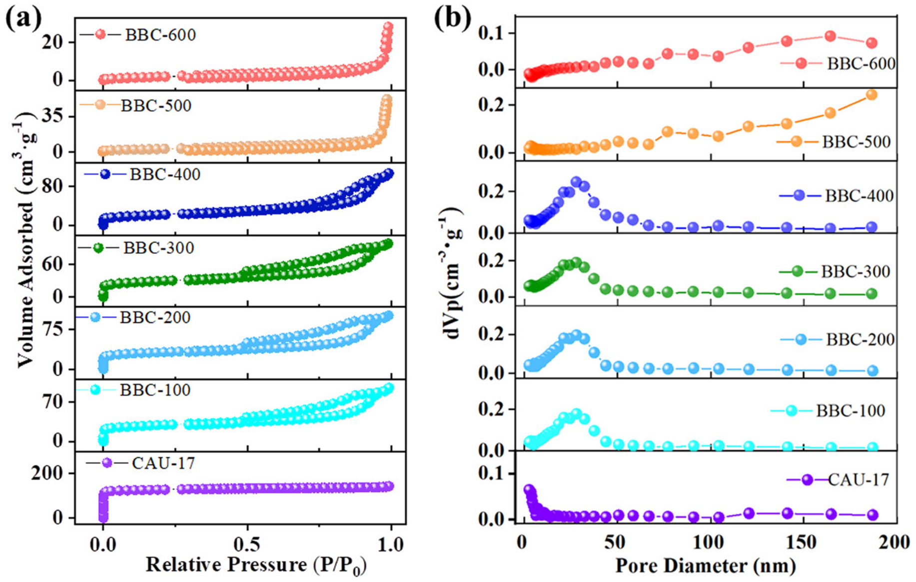

Fig. 5 (a) N_2 adsorption–desorption isotherms and (b) pore-size distribution of CAU-17, BBC-100, BBC-200, BBC-300, BBC-400, BBC-500 and BBC-600.

atmosphere, more carbon was oxidized, and the larger pores were formed, which was the reason for the gradually decreased specific surface area as the switching atmosphere temperature increased. This further confirmed the important role of the carbon skeleton structure in improving the specific surface area and adsorption capacity. In addition, BBC-500 and BBC-600 have macroporous and non-porous structures with type-III adsorption isotherms, which could be responsible for their small specific surface area (BBC-500: 10.47 m^2 g^{-1}, BBC-600: 8.832 m^2 g^{-1}) and poor adsorption capacity.

The optical response of the samples was evaluated by UV-vis DRS. As shown in Fig. 6, the higher the atmosphere switching temperature, the weaker the photoresponse of pyrolysis products. In particular, when the initial atmosphere switching temperature was lower than 400 °C, the light absorption of the Bi/β-Bi_2O_3@carbon photocatalysts (BBC-100, BBC-200, BBC-300, BBC-400) increased significantly due to the presence of a more non-oxidized carbon matrix. When the atmosphere switching temperature rose to 500 °C, the absorption band edge of the obtained BBC-500 sample was located at 558 nm. In addition, the appearance of two absorption band edges in BBC-600 was related to the coexistence of the α-Bi_2O_3 phase and β-Bi_2O_3 phase. The bandgap energies (E_g) were estimated based on Tauc plots ($(\alpha h\nu)^2 = A(h\nu - E_g)$).[41] As shown in Fig. 6b, compared with CAU-17, the E_g values of pyrolysis products obviously reduced. These results indicated that the pyrolysis treatment could significantly promote the absorption and conversion of sunlight, which was conducive to the improvement of the catalytic activity of the materials.

3.3 Photocatalytic degradation of FWA 351 by Bi/β-Bi_2O_3@carbon

The degradation of FWA 351 (10 mg L^{-1}) in aqueous solution (25 °C, initial pH 5.5) was selected to investigate the photocatalytic activity of the as-synthesized samples. For comparison, the degradation of FWA 351 by commercial Bi_2O_3 was also investigated under the same conditions.

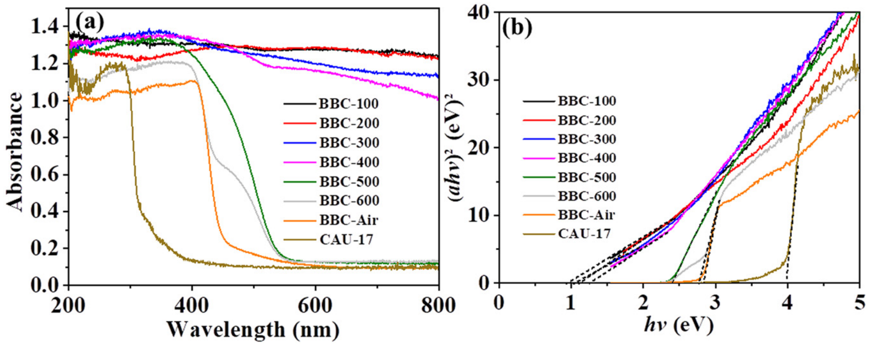

Fig. 6 (a) UV-vis DRS spectra of the samples and (b) plots of $(ah\nu)^2$ *vs.* photon energy of the samples.

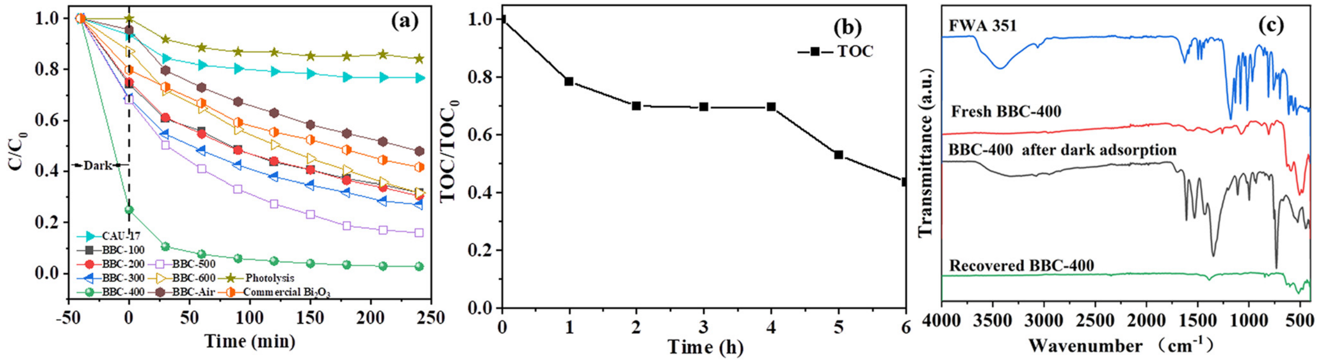

Fig. 7 (a) Photocatalytic degradation of FWA 351 by CAU-17, Bi/β-Bi_2O_3@carbon photocatalyst and commercial Bi_2O_3; (b) evolution of total organic carbon with illumination time; (c) FT-IR spectra of FWA 351, BBC-400, BBC-400 after dark adsorption and recovered BBC-400.

Fig. 7a shows the evolution of FWA 351 concentration with illumination time. It could be seen that the photocatalytic performance of CAU-17 was quite poor, and only 18% of FWA 351 could be degraded within 4 h. By contrast, the photocatalytic activity of the pyrolyzed materials was obviously improved. With the increase of the atmosphere switching temperature, the performance of the pyrolyzed materials first increased and then decreased, with BBC-400 having the best performance, for which the degradation efficiency for FWA 351 reached 89% within 4 h.

The removal efficiency of the total organic carbon (TOC) was further measured to evaluate the potential secondary pollution hazards in the FWA 351 degradation process. As shown in Fig. 7b, the TOC removal rate could reach 60% within 6 h. It was worth noting that the TOC removal efficiency did not change significantly within 2–4 hours of light illumination, indicating that the intermediate product formed in this period was relatively stable. With a prolonged light duration, the TOC began to decrease gradually, suggesting that the intermediates could be further degraded until FWA 351 was completely mineralized. To confirm that the elimination and mineralization of FWA 351 was not due to the adsorption of FWA 351 or its by-products on the catalyst surface, the FT-IR spectra of FWA 351, fresh BBC-400, BBC-400 after dark adsorption and the recovered BBC-400 were obtained. The results are shown in Fig. 7c. It could be seen that the characteristic peaks of FWA 351 were blue shifted after dark adsorption, indicating that there was a strong interaction between FWA 351 and BBC-400. These characteristic peaks of FWA 351 disappeared in the FT-IR spectrum of the recovered BBC-400, confirming that FWA

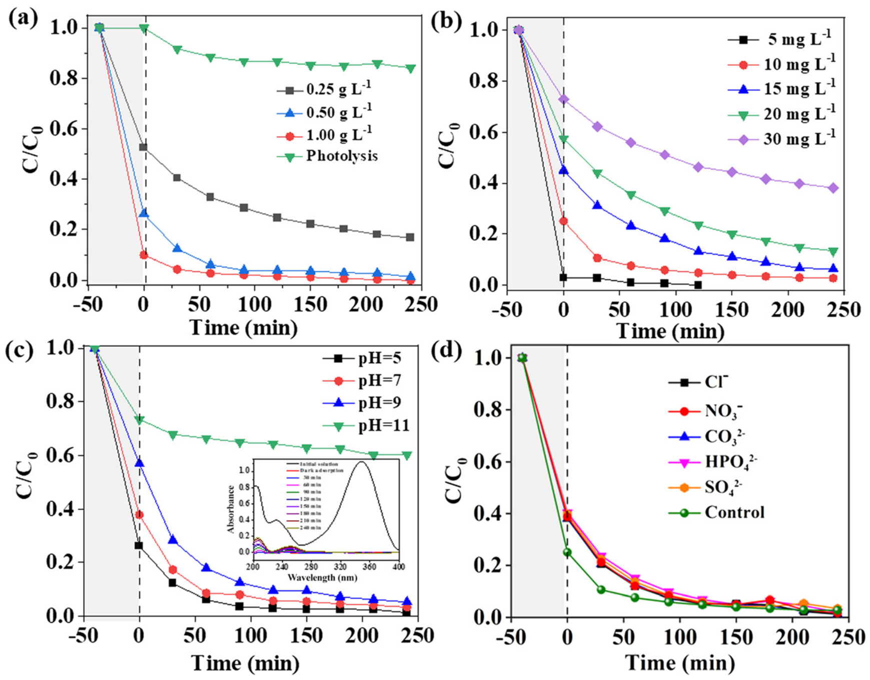

Fig. 8 Effects of various parameters on the degradation of FWA 351: (a) FWA 351 concentration, (b) dosage of the photocatalyst, (c) pH and (d) anions.

351 was removed by effective degradation rather than by surface adsorption of the material.

3.4 Effects of reaction conditions on the degradation of FWA 351

Fig. 8 shows the influence of various operating parameters on the removal of FWA 351 by BBC-400 under simulated sunlight irradiation. As shown in Fig. 8a, photolysis in the absence of a photocatalyst resulted in only a slight reduction in the concentration of FWA 351. The reason may be due to the chemical reaction of the C═C bonds in the structure under light irradiation, but the aromatic ring-opening is difficult. To further verify the conclusion, the TOC values of FWA 351 before and after photolysis were measured, and the results showed that the mineralization was negligible (1.6%, 6 h). Nevertheless, when a small amount of catalyst (0.25 g L^{-1}) was added, the removal efficiency for FWA 351 was significantly improved, indicating that photocatalysis was the main reason for the decrease of the concentration of FWA 351. With the increase of catalyst dosage, the adsorption and removal efficiency of FWA 351 increased. The reason was that more photocatalysts could provide more adsorption and catalytic reaction sites, which were conducive to the photocatalytic removal of pollutants. When the dosage of the photocatalyst was 0.5 g L^{-1}, satisfactory removal efficiency could be achieved. Further increasing the dosage of BBC-400 did not significantly improve the degradation efficiency due to the fact that excessive photocatalyst would increase the light scattering and reduce the effective utilization of light. Considering the application cost, the optimal dosage of the photocatalyst was determined to be 0.5 g L^{-1}. The effect of the concentration of FWA 351 on the removal efficiency is shown in Fig. 8b. It could be seen that BBC-400 had a robust ability to degrade FWA351 even at higher concentration (20 mg L^{-1}, 30 mg L^{-1}), and the degradation efficiency reached 77% and 48% within 4 h, respectively. At lower concentration (5 mg L^{-1}), FWA 351 could be completely degraded within 2 h.

The influence of pH on the degradation of FWA 351 was investigated. As seen in Fig. 8c, in the range of pH 5.0–9.0, the degradation efficiency increased with the decrease of the pH value. The reason was that the pH value affected the photocatalytic activity in different ways. For instance, the pH value not only affected the surface charge properties of the photocatalyst in solution, but also determined the existing forms of the target pollutant, which ultimately affected the adsorption capacity of the photocatalyst for the target pollutant and the subsequent interfacial reaction. The measured zeta potential (−36.1 eV) indicated that the surface of the Bi/β-Bi_2O_3@carbon composite photocatalyst was negatively charged. In addition, since FWA351 is a derivative

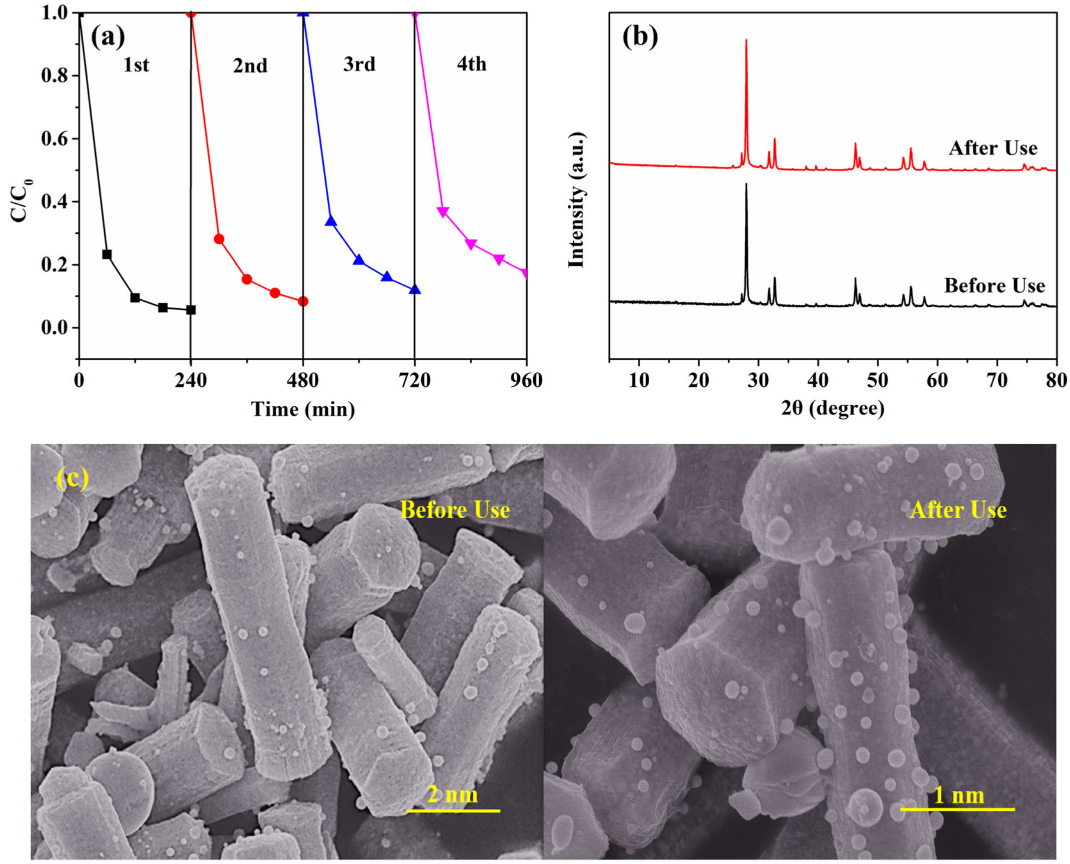

Fig. 9 (a) Reuse of BBC-400 in removing FWA 351; (b) XRD patterns and (c) SEM images of BBC-400 before and after four cycles of reuse.

of sodium sulfonate, its pK_a value is as low as −0.92,[42] indicating that FWA351 exists in the form of an anion under the experimental conditions. Therefore, FWA351 had the same charge properties as BBC-400, and there was electrostatic repulsion between BBC-400 and FWA351. As the pH value increased from 5.0 to 11, the electrostatic repulsion was enhanced, resulting in a significant decrease in the adsorption of the target substance, which was one of the important reasons for its poor pollutant removal efficiency at a higher pH value. In addition, holes could oxidize hydroxyl radicals to form hydroxyl radical active substances. The formation of hydroxyl radical was also affected by the pH value. It should be noted that when the pH value was adjusted to 3.0, the characteristic peak of FWA 351 at 348 nm completely disappeared after dark adsorption. Since FWA 351 was stable in acid media, it could be concluded that the decrease of the FWA 351 concentration in the dark adsorption stage was due to the adsorption rather than the decomposition of FWA 351. However, a new absorption peak appeared at 251 nm after illumination, and the peak intensity increased gradually with the extension of illumination time. The reason was that FWA 351 adsorbed on the catalyst surface was degraded and the resulting intermediates were further desorbed into the solution. In particular, common anions in water had little effect on the photocatalytic reaction process (Fig. 8d), indicating that the BBC-400 photocatalyst had excellent anti-interference ability for the degradation of FWA 351.

3.5 Reusability and stability

To further evaluate the stability and reusability of the material, the recycling tests were performed. The BBC-400 powder was recovered after the photocatalytic reaction and reused four times. The result showed that the photocatalytic activity of BBC-400 was only slightly reduced, and 83% of FWA 351 was removed after four consecutive cycles (Fig. 9a). The mineralization efficiencies for FWA-351 during the recycling were measured, and the results are shown in Fig. S2.† It could be seen that the mineralization efficiency for FWA351 of the first three cycles exceeded 56.7%, and mineralization efficiency dropped to 25.7% after the fourth cycle. The loss of photocatalysts caused by the recovery process and the partial occupation of active sites by small molecular intermediates that were not mineralized in time may be the main reasons for the significant decrease in mineralization efficiency after the fourth cycle. In addition, XRD and SEM images of fresh and the recovered BBC-400 showed no remarkable change in the material (Fig. 9b and c), indicating that the Bi/β-Bi_2O_3@carbon photocatalyst prepared had excellent stability and durability for reuse. In addition, considering the risk of secondary contamination caused by the release of the metal ions from the photocatalyst, the leaching of bismuth ions were investigated. After exposure to light for 2 h, 4 h and 6 h, respectively, the photocatalyst particles were removed with 0.22 μm ANPEL polyethersulfone membrane filters (China), and the bismuth ions in the supernatant were analyzed by ICP-MS. The results showed that no bismuth ions were detected in the samples, which proved that the Bi/β-Bi_2O_3@carbon photocatalyst prepared in the present work had satisfactory stability. These further confirm that the Bi/β-Bi_2O_3@carbon photocatalyst had good practical application prospect.

3.6 Photocatalytic mechanism

3.6.1 Photoelectric performance evaluation. The photocurrents were measured to explore the mechanism of promoting the performance of the materials. Fig. 10a shows that with the increase of atmosphere switching temperature, the photocurrent density first increased and then decreased, and BBC-400 exhibited the highest photocurrent density. In addition, the smallest Nyquist semicircular diameter of BBC-400 and BBC-600 in electrochemical impedance spectroscopy (EIS) also confirmed their lowest charge transfer resistance (Fig. 10b), which meant rapid charge transfer and high current density.[33] It was worth noting that although the impedance of BBC-600 was similar to that of BBC-400, the photocurrent density of BBC-600 was significantly lower than

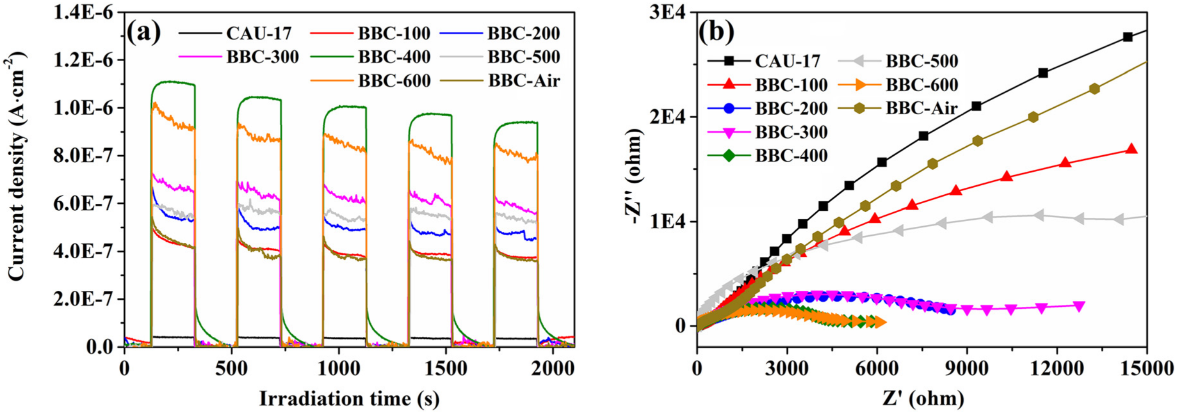

Fig. 10 (a) Photocurrent responses and (b) EIS Nyquist plots of CAU-17, BBC-air and Bi/β-Bi_2O_3@carbon photocatalysts.

that of BBC-400. The reason was related to the different contents of the crystal phase structure and component in the photocatalysts obtained at different atmosphere switching temperatures. For instance, with the increase of the initial atmosphere switching temperature, the content of metal bismuth first increased and then decreased, while the amount of carbon and Bi_2O_3 gradually decreased and increased, respectively. When the temperature was 400 °C, the obtained BBC-400 contained metal bismuth, β-Bi_2O_3 and carbon components, and the composition proportion achieved was the best under these conditions. The best performance was attributed to the improved visible light utilization resulted from the reduced bandgap of Bi/β-Bi_2O_3@carbon and the surface plasmon resonance effect of bismuth metal, as well as the facilitated interfacial electron migration and charge carrier separation through multi-interface transfer paths. However, when the temperature was increased to 600 °C, metal bismuth and carbon in the material were completely oxidized, and the above-mentioned synergistic effects were significantly weakened. In addition, the lowest peak PL intensity confirmed that BBC-400 had the lowest electron/hole recombination (Fig. S3†), which was related to the effective separation and transfer of charge carriers through multi-interface paths formed by carbon, metallic bismuth and bismuth oxide. In addition, the high activity β-Bi_2O_3 formed in BBC-600 was responsible for the higher photocurrent of BBC-600 than that of the BBC-air sample.[43]

3.6.2 Identification of active substances. The active substances of the photocatalytic reaction were determined by trapping experiments. Herein, EDTA-2Na, $AgNO_3$, *p*-benzoquinone (BQ) and isopropanol (IPA) separately acted as trapping agents for holes (h^+), electrons (e^-), superoxide radicals ($\cdot O_2^-$) and hydroxyl radicals ($\cdot OH$). In addition, because the amount of the capture agent added has a large effect on the photocatalytic reaction, the amount of scavengers added was set at the same level (1 mmol L^{-1}) to make a reliable comparison. Fig. S4† shows that the inhibition sequence of trapping agents on the degradation of FWA351 was EDTA-2Na > BQ > $AgNO_3$ > IPA, indicating that the effect of active substances on the degradation of FWA 351 was as follows: $h^+ > \cdot O_2^- > \cdot OH$.

The previous characterization results indicated that β-Bi_2O_3 was the main component of the composite photocatalyst, and its more positive valence band endowed the holes with superior oxidation ability. Therefore, it could oxidize pollutants either directly through hole oxidation or indirectly through hydroxyl radicals produced by hole oxidation of water molecules and hydroxyl ions. In addition, the low concentration of OH^- in natural water and its competitive adsorption with FWA351 could explain the reasons for the relatively small amount of hydroxyl radicals. Furthermore, the precious metal-like properties of bismuth in the photocatalyst accelerated the migration of electrons from the conduction band of β-Bi_2O_3 to Bi, and further reduced O_2 in water to produce $\cdot O_2^-$. To elucidate the photocatalytic mechanism theoretically, an empirical method was further used to calculate the band structure of the material. From the previous analysis, it could be inferred that the composition of BBC-500 was almost pure β-Bi_2O_3, so representative BBC-500 was selected for the calculation. According to the empirical equations: $E_{VB} = X - E^e + 0.5E_g$, $E_{CB} = E_{VB} - E_g$. Herein, X is 5.957 eV for β-Bi_2O_3. E^e is 4.5 eV. E_g is 2.44 eV for β-Bi_2O_3. Therefore, the E_{VB} and E_{CB} of β-Bi_2O_3 were 2.67 eV and 0.23 eV, respectively. Because the E_{CB} of β-Bi_2O_3 (0.23 eV) was significantly positive compared to the redox potential of $\cdot O_2^-/O_2$ (−0.33 eV),[8] it was inferred that the generation of $\cdot O_2^-$ was due to the plasma resonance effect of metal bismuth. In addition, the E_{VB} of β-Bi_2O_3 (2.67 eV) was obviously more positive than the redox potential of $\cdot OH/OH^-$ (1.99 eV),[44] which confirmed that β-Bi_2O_3 has a strong ability to oxidize OH^- to produce $\cdot OH$.

3.6.3 Proposed photocatalytic mechanism. According to above results, the mechanism of the photocatalytic degradation of FWA 351 by the Bi/β-Bi_2O_3@carbon photocatalyst was proposed. As depicted in Scheme 2, FWA 351 adsorbed on the carbon skeleton reacted with the holes of β-Bi_2O_3, superoxide radicals produced by electron reduction of oxygen molecules on Bi components, and a small amount of hydroxyl radicals, respectively. These electron-deficient active species attacked the FWA351 molecule, resulting in the breaking of C═C bonds and the opening of the aromatic rings, and ultimately completely mineralizing into carbon dioxide, water and inorganic salts. The multiple functions of each component and their synergistic interactions could explain the enhancement of photocatalytic activity. For instance, the C-frame in the Bi/β-Bi_2O_3@carbon photocatalyst not only enhanced the adsorption of target pollutants, but also promoted the separation and transfer of electrons. Moreover, the surface plasmon resonance effect of bismuth metal endowed it with a dual function of promoting visible light absorption and carrier separation. The deep valence band location of the Bi_2O_3 photocatalyst contributed to the direct hole oxidation and the indirect oxidation of hydroxyl radicals to degrade pollutants.

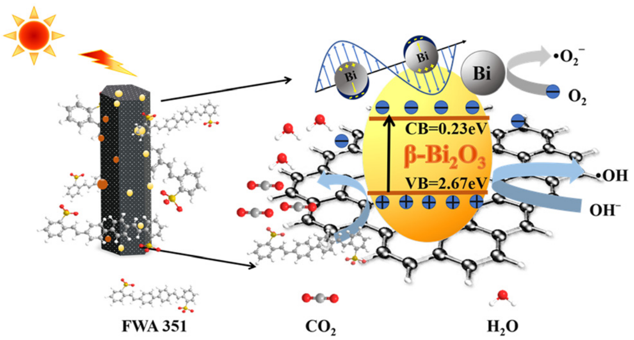

Scheme 2 Schematic diagram for the degradation of FWA 351 by the Bi/β-Bi_2O_3@carbon photocatalyst.

4. Conclusion

In summary, the Bi/β-Bi_2O_3@carbon photocatalyst was successfully prepared by MOF pyrolysis, and the crystal phase structure and components in the composite photocatalyst were easily regulated by simply switching the atmosphere when cooled to different temperatures. The strategy reported here has the advantages of easy operation, low energy consumption and environmental friendliness, through which problems such as difficult preparation, insufficient photoresponse range and unsatisfactory electron migration of metastable β-Bi_2O_3 were effectively solved. It was found that the optimal photocatalyst BBC-400 could completely remove FWA 351 (10 mg L^{-1}) in water within 4 h, and the mineralization efficiency reached 60% in 6 h. The enhancement of activity was attributed to the synergistic effects of improved visible light utilization resulted from the reduced bandgap of Bi/β-Bi_2O_3/carbon and the surface plasmon resonance effect of bismuth metal, as well as the facilitated interfacial electron migration and charge carrier separation through multi-interface transfer paths. Furthermore, 83% FWA 351 could be degraded after four consecutive cycles. The high activity, excellent stability and recyclability of Bi/β-Bi_2O_3@carbon confirmed its potential for future application in wastewater treatment.

Data availability

The data that support the findings of this study are available from the corresponding author upon reasonable request.

Author contributions

Xia Zhang: methodology, validation, and writing – original draft. Yifang Zhang: data curation and investigation. Xitong Yang: data curation and visualization. Jiaxin Han: visualization. Guifen Zhu: formal analysis. Jing Fan: supervision, project administration, and writing – review & editing.

Conflicts of interest

There are no conflicts to declare.

Acknowledgements

This work was supported by the National Natural Science Foundation of China (grant number 21777038) and the Key Scientific Research Projects of Colleges and Universities in Henan Province (grant number 22A610003).

References

1 I. Castro, E. Ekinci, X. Huang, H. A. Cheaito, Y. H. Ahn, J. Olivero-Verbel and Q. P. Dou, Proteasome-associated cysteine deubiquitinases are molecular targets of environmental optical brightener compounds, *J. Cell. Biochem.*, 2019, **120**, 14065–14075.

2 L. Zeng, X. Han, S. Pang, J. Ge, Z. Feng, J. Li and B. Du, Nationwide occurrence and unexpected severe pollution of fluorescent brighteners in the sludge of china: An emerging anthropogenic marker, *Environ. Sci. Technol.*, 2023, **57**, 3156–3165.

3 H. Chen, X. Han, C. Zhu, B. Du, L. Tan, R. He, M. Shen, L. Y. Liu and L. Zeng, Identification of fluorescent brighteners as another emerging class of abundant, ubiquitous pollutants in the indoor environment, *Environ. Sci. Technol.*, 2022, **56**, 10131–10140.

4 T. T. Ayeni, Y. Iwamoto, K. Takeda, H. Sakugawa and K. M. G. Mostofa, Optical properties of dissolved organic matter in Japanese rivers and contributions to photoformation of reactive oxygen species, *Sci. Total Environ.*, 2022, **826**, 153671.

5 S. Mapara, U. D. Patel, O. Keen and J. P. Ruparelia, Significant improvement in biodegradability of a real Optical Brightening Agent (OBA) wastewater using small doses of Fenton's reagent, *Environ. Technol.*, 2019, **42**, 2112–2121.

6 S. Ryu, S. Lee, H. Oh, S. Oh, M. Park, J. Kim and J. Heo, Study on the removal of fluorescent whitening agent from paper-mill wastewater using the submerged membrane bioreactor (SMBR) with ozone oxidation process, *Processes*, 2021, **9**, 1068.

7 A. Bouziani, M. Yahya, C. L. Bianchi, E. Falletta and G. Celik, Ternary polyaniline@Bi_2O_3-BiOCl nanocomposites as innovative highly active photocatalysts for the removal of the dye under solar light irradiation, *Nanomaterials*, 2023, **13**, 13040713.

8 T. Kanagaraj, P. S. Murphin Kumar, R. Thomas, R. Kulandaivelu, R. Subramani, R. N. Mohamed, S. Lee, S. W. Chang, W. J. Chung and D. D. Nguyen, Novel pure alpha-, beta-, and mixed-phase alpha/beta-Bi_2O_3 photocatalysts for enhanced organic dye degradation under both visible light and solar irradiation, *Environ. Res.*, 2022, **205**, 112439.

9 Y. Wang, C. Ban, Y. Feng, J. Ma, J. Ding, X. Wang, L. Ruan, Y. Duan, M. G. Brik, L. Gan and X. Zhou, Unveiling the synergistic role of nitrogen vacancies and Z-scheme heterojunction in g-C_3N_4/β-Bi_2O_3 hybrids for enhanced CO2 photoreduction, *Nano Energy*, 2024, **124**, 109494.

10 C. Zhao, C. Wang, X. Ren, S. Yuan, L. Zhao, L. Zhuang, B. Teng, Y. Wu and Y. He, Heterophase structure of $ZnSnO_3$ (rhombohedral and orthorhombic) for efficient dye degradation and N_2-to-NH_3 conversion via piezocatalysis and piezo-photocatalysis, *Chem. Eng. J.*, 2024, **498**, 155202.

11 S. Dong, L. Cui, Y. Tian, L. Xia, Y. Wu, J. Yu, D. M. Bagley, J. Sun and M. Fan, A novel and high-performance double Z-scheme photocatalyst ZnO-SnO_2-Zn_2SnO_4 for effective removal of the biological toxicity of antibiotics, *J. Hazard. Mater.*, 2020, **399**, 123017.

12 O. M. Yaghi, G. Li and H. Li, Selective binding and removal of guests in a microporous metal–organic framework, *Nature*, 1995, **378**, 703–706.

13 H. B. Truong, V. N. Le, M. N. Zafar, I. Rabani, H. H. Do, X. C. Nguyen, V. K. Hoang Bui and J. Hur, Recent advancements in modifications of metal–organic

frameworks-based materials for enhanced water purification and contaminant detection, *Chemosphere*, 2024, **356**, 141972.

14 B. Liu, H. Shioyama, T. Akita and Q. Xu, Metal organic framework as a template for porous carbon synthesis, *J. Am. Chem. Soc.*, 2008, **130**, 5390–5391.

15 P. C. Nagajyothi, R. Ramaraghavulu, K. Pavani and J. Shim, Catalytic reduction of methylene blue and rhodamine B using Ce-MOF-derived CeO_2 catalyst, *Mater. Lett.*, 2023, **336**, 133837.

16 E. Doustkhah, M. Esmat, N. Fukata, Y. Ide, D. A. H. Hanaor and M. H. N. Assadi, MOF-derived nanocrystalline ZnO with controlled orientation and photocatalytic activity, *Chemosphere*, 2022, **303**, 134932.

17 B. Deng, H. Song, K. Peng, Q. Li and J. Ye, Metal-organic framework-derived Ga-Cu/CeO_2 catalyst for highly efficient photothermal catalytic CO_2 reduction, *Appl. Catal., B*, 2021, **298**, 120519.

18 N. D. Kolhe, L. S. Walekar, A. N. Kadam, A. S. Chopade, S.-W. Lee, D. S. Mhamane, S. N. Shringare, A. S. Lawand, G. S. Gokavi, M. Misra and M. G. Mali, MOF derived in-situ construction of core-shell Z-scheme $BiVO_4$@α-Fe_2O_3-CF nanocomposites for efficient photocatalytic treatment of organic pollutants under visible light, *J. Cleaner Prod.*, 2023, **420**, 138179.

19 R. R. Salunkhe, Y. V. Kaneti and Y. Yamauchi, Metal-organic framework-derived nanoporous metal oxides toward supercapacitor applications: progress and prospects, *ACS Nano*, 2017, **11**, 5293–5308.

20 S. Thimmarayan, H. Mohan, B. M. K. Vasamsetti, G. Kim, K. Natesan, A. Jayaprakash and T. Shin, Ni/Co/Carbon nitride derived from ZIF-67 (MOF) nanocomposite: Enhanced light-driven photocatalytic degradation of methylparaben, mechanism & toxicity, *Chemosphere*, 2024, **347**, 140680.

21 Y. Chu, C. Zhao, Y. Zheng, X. Ren, S. Yuan, L. Zhao, Y. Wu and Y. He, $ZnSnO_3$-derived $ZnSnO_3$/ZIF-8 composites with enhanced adsorption and photocatalytic activity in RhB degradation and CO_2 reduction, *J. Environ. Sci.*, 2024, DOI: **10.1016/j.jes.2024.08.033**.

22 R. Das, P. Pachfule, R. Banerjee and P. Poddar, Metal and metal oxidenanoparticle synthesis from metal organic frameworks (MOFs): finding the border of metal and metal oxides, *Nanoscale*, 2012, **4**, 591–599.

23 L. Zhang, X. Zhou, S. Liu, H. Liu, S. Zhu, Y. Mao, Q. Yang, S. Zhu, C. Zhang, T. Wang and C. Wang, Two birds, one stone: Rational design of Bi-MOF/g-C_3N_4 photocatalyst for effective nitrogen fixation and pollutants degradation, *J. Cleaner Prod.*, 2023, **425**, 138912.

24 K. Cao, F. He, J. Yan, W. Zhu, Y. Wang, Y. Zhang, B. Zhang, X. Yu, Q. Shen, C. Liu and Q. Wang, MOF-derived Bi@C nanocomposites electrode simultaneous detection of hydroquinone and catechol, *Inorg. Chem. Commun.*, 2023, **148**, 110327.

25 P. Zhang, Y. Wei, S. Zhou, R. A. Soomro, M. Jiang and B. Xu, A metal-organic framework derived approach to fabricate in-situ carbon encapsulated Bi/Bi_2O_3 heterostructures as high-performance anodes for potassium ion batteries, *J. Colloid Interface Sci.*, 2023, **630**, 365–374.

26 H. Ouyang, N. Chen, G. Chang, X. Zhao, Y. Sun, S. Chen, H. Zhang and D. Yang, Selective capture of toxic selenite anions by bismuth-based metal–organic frameworks, *Angew. Chem., Int. Ed.*, 2018, **57**, 13197–13201.

27 A. K. Inge, M. Köppen, J. Su, M. Feyand, H. Xu, X. Zou, M. O'Keeffe and N. Stock, Unprecedented topological complexity in a metal–organic framework constructed from simple building units, *J. Am. Chem. Soc.*, 2016, **138**, 1970–1976.

28 L. Wang, P. Tang, J. Liu, A. Geng, C. Song, Q. Zhong, L. Xu and L. Gan, Multifunctional ZnO-porous carbon composites derived from MOF-74(Zn) with ultrafast pollutant adsorption capacity and supercapacitance properties, *J. Colloid Interface Sci.*, 2019, **554**, 260–268.

29 S. Majumder, N. D. Quang, T. Thi Hien, N. D. Chinh, H. Yang, C. Kim and D. Kim, Nanostructured β-Bi_2O_3/PbS heterojunction as np-junction photoanode for enhanced photoelectrochemical performance, *J. Alloys Compd.*, 2021, **870**, 159545.

30 X. Yang, Y. Zhang, Y. Wang, C. Xin, P. Zhang, D. Liu, B. B. Mamba, K. K. Kefeni, A. T. Kuvarega and J. Gui, Hollow β-Bi_2O_3@CeO_2 heterostructure microsphere with controllable crystal phase for efficient photocatalysis, *Chem. Eng. J.*, 2020, **387**, 124100.

31 W. Zhang, X. Jiang, X. Wang, Y. V. Kaneti, Y. Chen, J. Liu, J. S. Jiang, Y. Yamauchi and M. Hu, Spontaneous weaving of graphitic carbon networks synthesized by pyrolysis of ZIF-67 crystals, *Angew. Chem., Int. Ed.*, 2017, **56**, 8435–8440.

32 E. Zhang, T. Wang, K. Yu, J. Liu, W. Chen, A. Li, H. Rong, R. Lin, S. Ji, X. Zheng, Y. Wang, L. Zheng, C. Chen, D. Wang, J. Zhang and Y. Li, Bismuth single atoms resulting from transformation of metal–organic frameworks and their use as electrocatalysts for CO_2 reduction, *J. Am. Chem. Soc.*, 2019, **141**, 16569–16573.

33 H. A. L. Pham, D. T. Nguyen, V. C. Nguyen and T. Ky Vo, Integrating Bi-containing metal–organic frameworks for enhancing their LED visible-light-driven photocatalytic activities towards Rhodamine dye, *Inorg. Chem. Commun.*, 2024, **159**, 111822.

34 L. Bao, Q. Bao, W. Jiang and G. Xu, Hydrothermal synthesis of Bi@$Bi_4Ti_3O_{12}$ nanosheets with enhanced visible-light photocatalytic activity, *CrystEngComm*, 2020, **22**, 6316–6321.

35 H. Cheng, B. Huang, J. Lu, Z. Wang, B. Xu, X. Qin, X. Zhang and Y. Dai, Synergistic effect of crystal and electronic structures on the visible-light-driven photocatalytic performances of Bi_2O_3 polymorphs, *Phys. Chem. Chem. Phys.*, 2010, **12**, 15468.

36 X. Yu, Q. Feng, D. Ma, H. Lin, Z. Liu, Y. Huang, X. Huang, X. Dong, Y. Lei and D. Wang, Facile synthesis of α/β-Bi_2O_3 hetero-phase junction by a solvothermal method for enhanced photocatalytic activities, *Mol. Catal.*, 2021, **503**, 111431.

37 J. Yan, H. Wang, B. Jin, M. Zeng and R. Peng, Cu-MOF derived Cu/Cu_2O/C nanocomposites for the efficient thermal

decomposition of ammonium perchlorate, *J. Solid State Chem.*, 2021, **297**, 122060.

38 M. Zhang, Y. Qin, F. Zhang, Y. Feng, S. N. Ozer, W. Sun, Y. Zhao and Z. Xu, Site-selective etching and conversion of bismuth-based metal–organic frameworks by oxyanions enables efficient and selective adsorption via robust coordination bonding, *Chem. Eng. J.*, 2024, **488**, 150867.

39 D.-H. Zhuo, Q.-S. Chen, X.-H. Zhao, Y.-L. Jiang, J. Lu, Z.-N. Xu and G.-C. Guo, Ce-doped Bi based catalysts for highly efficient electroreduction of CO_2 to formate, *J. Mater. Chem. C*, 2021, **9**, 7900–7904.

40 A. Wang, Z. Zheng, H. Wang, Y. Chen, C. Luo, D. Liang, B. Hu, R. Qiu and K. Yan, 3D hierarchical H_2-reduced Mn-doped CeO_2 microflowers assembled from nanotubes as a high-performance Fenton-like photocatalyst for tetracycline antibiotics degradation, *Appl. Catal., B*, 2020, **277**, 119171.

41 Z. Wei, N. Zheng, X. Dong, X. Zhang, H. Ma, X. Zhang and M. Xue, Green and controllable synthesis of one-dimensional Bi_2O_3/BiOI heterojunction for highly efficient visible-light-driven photocatalytic reduction of Cr(VI), *Chemosphere*, 2020, **257**, 127210.

42 C. Wang, H. Yang, F. Li, P. Jin, W. Zhu and J. Fan, Efficient adsorption of fluorescent whitening agent 351 from high salinity environmental water by polymer supported hydroxyl functional ionic liquid, *Sep. Purif. Technol.*, 2024, **334**, 125901.

43 N. Channa, T. A. Gadhi, R. B. Mahar, A. Chiadò, B. Bonelli and A. Tagliaferro, Combined photocatalytic degradation of pollutants and inactivation of waterborne pathogens using solar light active α/β-Bi_2O_3, *Colloids Surf., A*, 2021, **615**, 126214.

44 D. Wang, X. Yu, Q. Feng, X. Lin, Y. Huang, X. Huang, X. Li, K. Chen, B. Zhao and Z. Zhang, In-situ growth of β-Bi_2O_3 nanosheets on g-C_3N_4 to construct direct Z-scheme heterojunction with enhanced photocatalytic activities, *J. Alloys Compd.*, 2021, **859**, 157795.